Anisotropic Organised Eddy Simulation for the prediction of non-equilibrium turbulent flows around bodies

R. Bourguet*, M. Braza, G. Harran, R. El Akoury

Institut de Mécanique des Fluides de Toulouse, 6 allée du Prof. C. Soula, 31400 Toulouse, France

Abstract

The unsteady turbulent flow around bodies at high Reynolds number is predicted by an anisotropic eddy-viscosity model in the context of the Organised Eddy Simulation (OES). A tensorial eddy-viscosity concept is developed to reinforce turbulent stress anisotropy, that is a crucial characteristic of non-equilibrium turbulence in the near-region. The theoretical aspects of the modelling are investigated by means of a phase-averaged PIV in the flow around a circular cylinder at Reynolds number 1.4×10^5. A pronounced stress–strain misalignment is quantified in the near-wake region of the detached flow, that is well captured by a tensorial eddy-viscosity concept. This is achieved by modelling the turbulence stress anisotropy tensor by its projection onto the principal matrices of the strain-rate tensor. Additional transport equations for the projection coefficients are derived from a second-order moment closure scheme. The modification of the turbulence length scale yielded by OES is used in the Detached Eddy Simulation hybrid approach. The detached turbulent flows around a NACA0012 airfoil (2-D) and a circular cylinder (3-D) are studied at Reynolds numbers 10^5 and 1.4×10^5, respectively. The results compared to experimental ones emphasise the predictive capabilities of the OES approach concerning the flow physics capture for turbulent unsteady flows around bodies at high Reynolds numbers.

1. Introduction

The accurate prediction of the unsteady loads induced by the interaction of turbulent flows with solid walls at high Reynolds number is a crucial issue in fluid–structure simulation. Since Direct Numerical Simulations of Navier–Stokes equations are still limited to low Reynolds numbers, the most popular approaches consist in splitting the physical variables into resolved and modelled parts and in simulating only mean quantities issued from an averaging or filtering procedure. The Large Eddy Simulation (LES) approach is based on a spatial filtering and leads to a distinction between resolved and modelled flow structures according to their size. Concerning wall flows, LES is still limited in the moderate Reynolds number range (Davidson et al., 2003). As a consequence, statistical approaches, as Unsteady Reynolds Averaged Navier–Stokes (URANS), are widespread and robust methodologies for the prediction of complex wall flows. However, classical URANS approaches use the same length and time scales of turbulence as in equilibrium flows in the sense of Kolmogorov's statistical theory and are characterised by excessive turbulence production rates that often

Corresponding author.
E-mail address: Remi.Bourguet@imft.fr (R. Bourguet).

doi:10.1016/j.jfluidstructs.2008.07.004

attenuate and damp unsteady instability modes (Jin and Braza, 1994; Durbin and Pettersson Reif, 2001). The benefits of URANS in near-regions and of LES in farther detached ones are associated in hybrid approaches. Especially, the Detached Eddy Simulation [DES, Travin et al. (2000)] does not need specified interfaces that create major defects in other hybrid approaches. DES attempts, as other approaches, to minimise excessive turbulence production rates in non-equilibrium turbulence regions and therefore avoiding damping of vortex structures that usually occurs by using classic URANS (Haase et al., 2006). However, standard DES often produces spurious separation regions because of equilibrium assumptions for the turbulence scales in the URANS regions. This creates high physical incoherences in matching the turbulence length scale with the LES regions (Haase et al., 2006; Peng and Haase, 2008).

To improve these aspects concerning the statistical and hybrid approaches, the Organised Eddy Simulation (OES) methodology can be considered (Bouhadji et al., 2002; Braza et al., 2006). OES distinguishes the structures to be resolved from those to be modelled on the basis of their organised (resolved part) or chaotic character (modelled part). The modelling of this part can be achieved by reconsidered URANS approach in respect of modified turbulence scales, by means of an appropriate physical modelling of the turbulent stresses. This has been achieved by using Differential Reynolds Stress transport Modelling (DRSM) to evaluate the eddy-diffusivity coefficient used in OES two-equation modelling (Bourdet et al., 2007). Therefore, this approach takes the benefits from DRSM and avoids its difficulties, mainly related to a numerically unstable character of the second-order closures and on their high computational cost.

This paper presents an improved modelling of the turbulent stresses in OES. Previous developments in OES had adopted Boussinesq (1877) behaviour law. In the present study, a tensorial eddy-viscosity concept is developed, by taking into account physical characteristics of a *directional* stress–strain misalignment. This approach is complementary to the attempts of modifying turbulence constitutive laws by means of scalar eddy-viscosity and by the use of higher-order tensors combining strain and vorticity tensors (Non-Linear Eddy-Viscosity Models, NLEVM, or Explicit Algebraic Reynolds Stress Models, EARSM [Pope, 1975; Shih et al., 1993; Gatski and Speziale, 1993; Speziale and Xu, 1996, for instance]). By the present approach, the lack of universality due to evaluation of new constants for the higher-order tensors in respect of the flow studied is avoided. The present paper is composed as follows. In Section 2, a physical analysis of stress–strain relations is performed on the basis of a detailed high Reynolds PIV experiment concerning the incompressible flow past a circular cylinder at Reynolds number 1.4×10^5 (Perrin et al., 2007). In Section 3, a methodology based on a directional eddy-viscosity concept is presented to capture stress–strain non-linearities yielding a new turbulent stress constitutive law. Transport equations for the new state variables involved in this constitutive law are derived. The predictive capabilities of this approach are examined in Section 4 by means of numerical simulation around a NACA0012 airfoil at 20° of incidence and Reynolds number 10^5. The ability of OES approach to improve DES is assessed by a numerical simulation of the incompressible 3-D flow past a circular cylinder compared to previous experimental results.

2. Physical analysis of turbulent stress–strain relation in the near-region

The relation between turbulent stress and mean strain-rate tensors is investigated on the basis of a detailed PIV experiment in the incompressible flow past a circular cylinder at high Reynolds number. The experiment has been carried out in the wind tunnel S1 of IMFT in the context of DESIDER European program. A complete description concerning the experimental setup and measurement techniques have been reported in Perrin et al. (2007). Only the main characteristics of the configuration are recalled here. The channel has a $670 \times 670\,\mathrm{mm}^2$ cross-section and the cylinder of diameter $D = 140\,\mathrm{mm}$ spans the width of the channel without endplates. It has a diameter D of 140 mm, giving an aspect ratio $L/D = 4.8$ and a high blockage coefficient $D/H = 0.208$, where L and H are channel width and height, respectively. The upstream velocity at the centre of the channel is 15 m/s. The Reynolds number based on the upstream velocity and on the cylinder diameter is 1.4×10^5. The free-stream turbulence intensity, measured by hot wire in the inlet is 1.5%. Three-component PIV has been performed (Perrin et al., 2007). The test-section plan has been considered at half distance spanwise and located in the near-wake region. The measurement domain is $x_1/D \in [0.6, 2.28]$ and $x_2/D \in [-0.52, 0.7]$. Phase-averaged decomposition is performed, due to the quite pronounced periodic character of the flow in respect of von Kármán vortex shedding. The Linear Stochastic Estimation has been employed to phase the three-component PIV snapshots (Perrin et al., 2007). In the following, all experimental quantities are phase-averaged and non-dimensional. The phase-average decomposition is expressed as follows: $U_i^{\mathrm{inst}} = \langle U_i^{\mathrm{inst}} \rangle + u_i$, where U_i^{inst} are instantaneous velocity components, $\langle \cdot \rangle$ denotes phase-averaging operator and u_i are velocity fluctuations; $\langle u_i u_j \rangle$ are the turbulent stresses. This experimental database enables a precise monitoring of phase-averaged and turbulent fields as Fig. 1 illustrates it. Therefore, this study can be used in the context of OES, as described in Section 3. Phase-averaged normal and shear turbulent stresses and turbulent kinetic energy ($k = \frac{1}{2}\langle u_\alpha u_\alpha \rangle$) are represented at a given phase angle

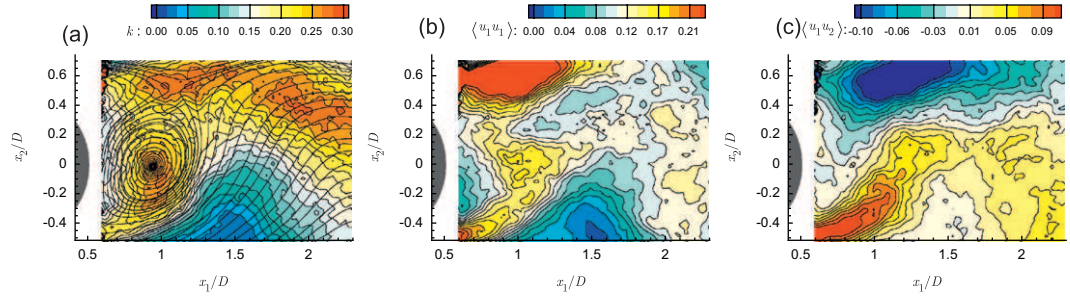

Fig. 1. Iso-contours of phase-averaged (a) turbulent kinetic energy, (b) normal $\langle u_1u_1\rangle$, (c) shear $\langle u_1u_2\rangle$ turbulent stresses at phase angle $\varphi = 50^\circ$. In (a) velocity streamlines are superimposed.

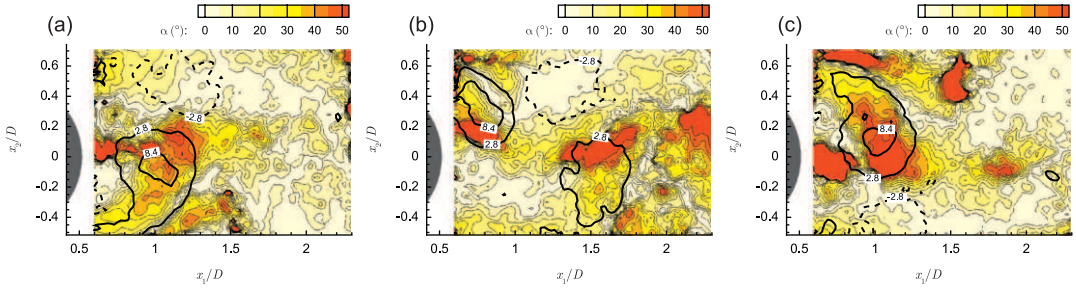

Fig. 2. Iso-contours of the angle between the first principal directions of $-\mathbf{a}$ and $\mathbf{S}$ at three given phase angles: (a) $\varphi = 50^\circ$, (b) $\varphi = 140^\circ$ and (c) $\varphi = 230^\circ$. Iso-lines of Q criterion (bold lines, dashed lines for $Q<0$).

($\varphi = 50^\circ$). Greek subscripts are used to specify implicit summations. A high level of turbulent kinetic energy is shown in the coherent structure regions as well as in high shear flow ones (Fig. 1(a)). In vortex advection region, the highest values of the normal stresses $\langle u_iu_i\rangle$ are located near the centre of the coherent structures (Fig. 1(b)) whereas high values of turbulent shear stress are reached near saddle points (Fig. 1(c)). In the very near-wake region, high values of shear and normal stresses are observed in the shear layers, as expected.

Boussinesq law assumes a linear relation between turbulent stress and mean strain-rate tensors. This can be written as follows, under incompressibility assumption:

$$-\frac{\langle u_iu_j\rangle}{k}+\frac{2}{3}\delta_{ij} = -a_{ij} = 2\frac{\nu_t}{k}S_{ij} \quad \text{with } \nu_t = \frac{C_\mu k^2}{\varepsilon}, \tag{1}$$

where δ_{ij} is Kronecker symbol. $\boldsymbol{a}$ denotes turbulent stress anisotropy tensor which is the traceless and non-dimensional form of turbulent stresses. $\mathbf{S}$ is the mean strain-rate tensor, defined by $S_{ij} = \frac{1}{2}(\partial U_i/\partial x_j + \partial U_j/\partial x_i)$, where $U_i = \langle U_i^{\text{inst}}\rangle$. The scalar eddy-viscosity ν_t is expressed by means of the turbulence length and time scales. ε is the turbulent kinetic energy dissipation rate and C_μ denotes an eddy-diffusivity coefficient. $\boldsymbol{a}$ and $\mathbf{S}$ being real symmetrical tensors, their eigenvectors form orthogonal basis. These are classified according to the corresponding eigenvalue decreasing magnitudes, λ_i^a and λ_i^S denoting $-\boldsymbol{a}$ and $\mathbf{S}$ ith eigenvalues, respectively. In the following, $\mathbf{v}_i^a$ and $\mathbf{v}_i^S$ are ith eigenvectors of $-\boldsymbol{a}$ and $\mathbf{S}$. The previously described phase-averaged PIV enables to access the complete anisotropy tensor but only strain tensor components which do not involve spatial gradients in x_3 direction. In the following, two-dimensionality assumption is made, taking into account the experimental setup symmetry. The angle between the first principal directions of the strain and anisotropy tensors is quantified at given phase angles (Fig. 2). The main coherent vortex regions are illustrated in Fig. 2 by a positive value of Q criterion, $Q = \frac{1}{2}((\partial U_\alpha/\partial x_\alpha)^2 - (\partial U_\alpha/\partial x_\beta)(\partial U_\beta/\partial x_\alpha))$ (Hunt et al., 1988).

As noticed in a preliminary study (Bourguet et al., 2007), a strong misalignment is observed in many regions. This emphasises the limitations of the linear EVM assuming that the principal directions of $-\boldsymbol{a}$ and $\mathbf{S}$ remain collinear. From a general point of view, strong non-collinearities appear near the vortex centre ($x_1/D = 1.1$, $x_2/D = 0.15$), ($x_1/D = 1.5$, $x_2/D = 0.05$) and ($x_1/D = 1.1$, $x_2/D = 0$) in Fig. 2(a), (b) and (c), respectively, as well as in high shear flow regions like in the upper shear layer in Fig. 2(c). However, $\mathbf{v}_1^a$ and $\mathbf{v}_1^S$ are also strongly misaligned in the near-wake region, close to $x_2/D = 0$. The best alignment is reached in farther free-shear flow regions and near saddle points located by negative

values of Q criterion, ($x_1/D = 1.3$, $x_2/D = 0.5$) in Fig. 2(b), for instance. The analysis of high misalignment zones allows locating precisely the validity regions of the linear isotropic law. In the perspective of an improvement of a turbulent stress constitutive relation, these structural properties have to be captured.

3. Anisotropic OES modelling

The present study aims at providing an efficient and robust turbulence modelling methodology for the prediction of non-equilibrium turbulent flows around bodies at high Reynolds number (order of 10^6 or higher). It is recalled that a pure LES approach would be prohibitive in this Reynolds number range because it would involve very fine grids in the near-region. The statistical turbulence modelling offers robustness of the simulations in this region at high Reynolds numbers but it has proven a strong dissipative character that tends to damp crucial instabilities occurring in turbulent flows around bodies, as for example low frequency modes as von Kármán instability, buffet or flutter phenomenon. The OES approach offers an alternative that combines robustness and capture of the above physical phenomena. This approach consists in splitting the energy spectrum in a first part that regroups the organised flow structures (resolved part) and a second part that includes the chaotic processes due to the random turbulence (to be modelled). In the time-domain, the spectrum splitting leads to phase-averaged Navier–Stokes equations (Jin and Braza, 1994). A schematic illustration of the OES approach is presented in Fig. 3.

The turbulence spectrum to be modelled is extended from low to high wavenumber range and statistical turbulence modelling considerations can be adopted inducing robustness properties. However, the use of standard URANS modelling is not sufficient in this case. In non-equilibrium turbulence, the inequality between turbulence production and dissipation rate modifies drastically the shape and slope of the turbulence spectrum in the inertial range (Fig. 3), comparing to the equilibrium turbulence, according to Kolmogorov's cascade (slope equals $-\frac{5}{3}$). This modification has been quantified by the experimental study mentioned in Section 2 (Braza et al., 2006). Therefore, the turbulence scales used in standard URANS modelling have to be reconsidered in OES, to capture the effects due to the non-linear interaction between the coherent structures and the random turbulence. In the context of the OES approach, a modification of the turbulence scales in two-equation models was achieved on the basis of the second-order moment closure (Launder et al., 1975; Bourdet et al., 2007). By using the Boussinesq law (1) as well as the dissipation rate and the turbulent stresses evaluated by DRSM, a reconsidered eddy-diffusivity coefficient was derived. It was shown that the C_μ values were lower (order of 0.02) than the equilibrium turbulence value ($C_\mu = 0.09$) in two-equation modelling. Furthermore, the turbulence damping near the wall needed also to be revisited because of the different energy distribution between coherent and random processes in non-equilibrium near-wall regions. A damping law with a less abrupt gradient than in equilibrium turbulence was suggested, $f_\mu = 1 - \exp(-0.0002y^+ - 0.000065y^{+2})$ (Jin and Braza, 1994); $y^+ = y_n U_\tau/\nu$ is a non-dimensional wall distance, y_n is the distance perpendicular to the wall and U_τ the friction velocity. The efficiency of the OES approach in 2-D and 3-D has been proven in a number of strongly detached high Reynolds number flows, especially around wings (Hoarau et al., 2006), as well as in the context of DES (El Akoury et al., 2007), as described in Section 4. In the present study, special attention is paid to the reinforcement of the turbulent stress anisotropy in the near-region by reconsidering the Boussinesq constitutive law.

3.1. Modelling of the turbulent stress anisotropy tensor

The previous analysis (Section 2) concerning stress–strain non-linearity illustrates the need for an anisotropic constitutive law. To include these structural properties, each directional contribution of the strain tensor is considered

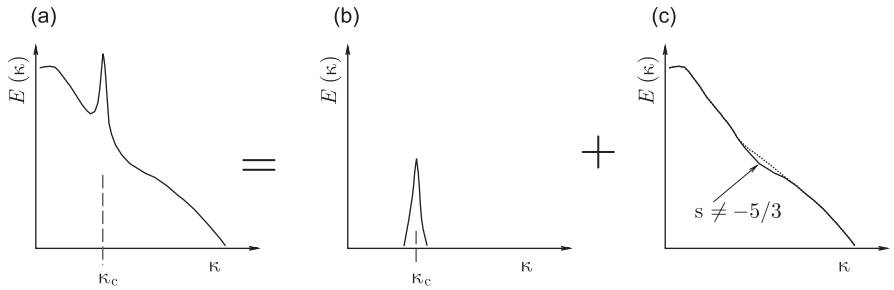

Fig. 3. Sketch of the energy spectrum splitting in OES: (a) energy spectrum, (b) coherent part (resolved) and (c) random, chaotic part (modelled). κ_c denotes coherent process wavenumber.

separately. A projection of the turbulence anisotropy tensor is performed onto the strain-rate principal matrices. This projection, $\hat{\boldsymbol{a}}$, is investigated in the generic linear form:

$$\hat{a}_{ij} = -C_{V\alpha} V^{\alpha}_{ij} \quad \text{with } C_{Vi} = -a_{\alpha\beta} V^{i}_{\alpha\beta} \text{ and } V^{i}_{\alpha\beta} V^{j}_{\alpha\beta} = \delta_{ij}. \tag{2}$$

$\mathbf{V}^i$ are 3×3 symmetrical tensors. C_{Vi} denotes the projection of $-\boldsymbol{a}$ onto $\mathbf{V}^i$. Under Boussinesq hypothesis, three tensors are considered ($\mathbf{V}^i = \mathbf{v}^S_i \mathbf{v}^{S\mathrm{T}}_i$, where $\cdot^{\mathrm{T}}$ denotes the transposition). The corresponding projection coefficients are approximated by $C_{Vi} \approx 2 v_t \lambda^S_i / k$. In the present study, the same basis tensors $\mathbf{V}^i$ are retained. These matrices of rank 1 are called $\mathbf{S}$ principal matrices in the following. Contrary to linear EVM, projection coefficients C_{Vi} are no more modelled but assumed to be predicted exactly as new state variables by DRSM transport equations. The methodology suggested here aims at capturing directional properties of stress–strain misalignments leading to an anisotropic constitutive law. C_{Vi} projection coefficients allow identification of directional misalignments (Fig. 4). These properties are not captured by the previous approaches.

Expression (2) with $\mathbf{V}^i = \mathbf{v}^S_i \mathbf{v}^{S\mathrm{T}}_i$ ensures that the modelling of the anisotropy tensor is symmetrical and traceless since $C_{V\alpha} = 0$. Moreover, the turbulent kinetic energy production term has the same form as in DRSM:

$$P_k = -k \hat{a}_{\alpha\beta} S_{\alpha\beta} = -k a_{\alpha\beta} S_{\alpha\beta}. \tag{3}$$

From expression (3), positive or even negative turbulent kinetic energy production regions are expected to be faithfully predicted, that is not the case when using linear EVM [e.g. Carpy and Manceau (2006)]. As a consequence of the projection subspace chosen here, the eigenvectors of $\hat{\boldsymbol{a}}$ are also eigenvectors of the strain tensor. The contribution of each principal matrix of the strain tensor is modulated according to the projection coefficient in each space direction. As shown in Fig. 5, the values of C_{Vi} are reduced in misalignment regions that reduces the influence of $\mathbf{V}^i$, whereas they remain maximum when the principal directions are aligned.

The projection coefficients are the eigenvalues of $\hat{\boldsymbol{a}}$. Therefore, no proportionality relation is assumed between stress and strain tensors as in linear EVM. This means that the sorting of $\hat{\boldsymbol{a}}$ and $\mathbf{S}$ eigenvectors may be different. Other basis tensors can be considered, especially those issued from NLEVM. The principal matrices of the strain tensor are retained here because these allow deriving transport equations for C_{Vi} coefficients as described in Appendix A.

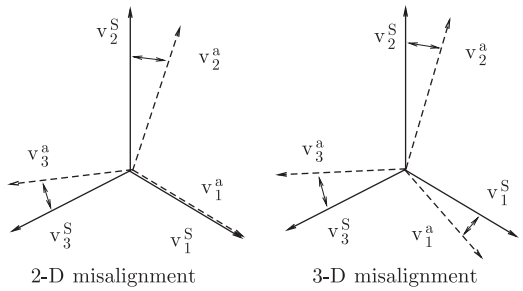

Fig. 4. Two cases of misalignment between turbulent stress anisotropy and mean strain-rate tensor eigenbasis.

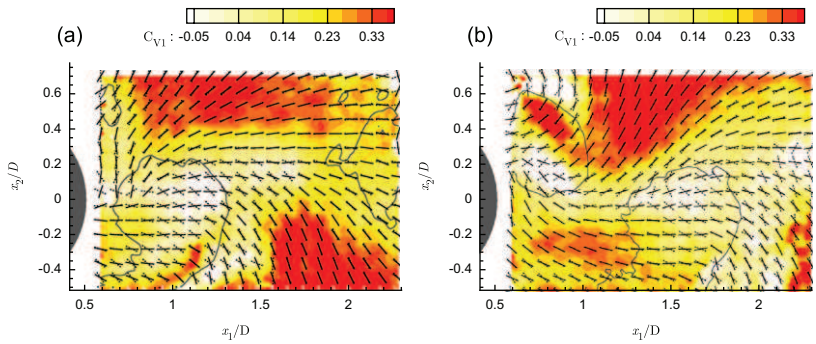

Fig. 5. Iso-contours of the first projection coefficient C_{V1} at two given phase angles, (a) $\varphi = 50°$ and (b) $\varphi = 140°$. $-\boldsymbol{a}$ (dashed) and $\mathbf{S}$ (solid) first principal directions are superimposed to locate high misalignment regions. Iso-contour of Q criterion $Q = 1$ is represented by dark grey lines.

3.2. Tensorial eddy-viscosity concept and constitutive law

The suggested modelling (2) for the turbulent stress anisotropy tensor can be expressed as an eddy-viscosity model by means of a generalisation of the scalar eddy-viscosity concept towards a tensorial definition $\boldsymbol{v}_{tt}$:

$$(v_{tt})_{ij} = (v_{td})_\alpha V^\alpha_{ij} \quad \text{with } (v_{td})_i = \frac{C_{Vi}}{2\lambda^S_i} k; \tag{4}$$

$(v_{td})_i$ is a directional eddy-viscosity vector. Furthermore, the following definition of an anisotropic eddy-diffusivity coefficient can be suggested by an extension of the scalar C_μ definition, $C_{\mu_i} = C_{Vi}/(2\eta_i)$. The quantities $\eta_i = k\lambda^S_i/\varepsilon$ can be regarded as directional expressions of $\eta = k\|S\|/\varepsilon$ that is the ratio of turbulent and mean flow time scales which emphasises the non-equilibrium turbulence regions (Speziale and Xu, 1996). The linear EVM behaviour law can be generalised as follows:

$$-\langle u_i u_j\rangle + \tfrac{2}{3}k\delta_{ij} = 2S_{i\alpha}(v_{tt})_{\alpha j} = 2(v_{td})_\alpha S^\alpha_{ij} \quad \text{with } S^m_{ij} = \lambda^S_m V^m_{ij}. \tag{5}$$

This anisotropic constitutive law involves the elements of a spectral decomposition applied to the mean strain-rate tensor, whose respective weights are determined by $(v_{td})_i$. Expression (5) leads to the following generalisation of the averaged Navier–Stokes momentum equations:

$$\frac{DU_i}{Dt} = \frac{\partial}{\partial x_\alpha}\left((\nu\delta_{\alpha\beta} + (v_{tt})_{\alpha\beta})\left(\frac{\partial U_i}{\partial x_\beta} + \frac{\partial U_\beta}{\partial x_i}\right) - \frac{2}{3}k\delta_{i\alpha}\right) - \frac{1}{\rho}\frac{\partial P}{\partial x_i}, \tag{6}$$

where ρ, P and ν are fluid density, pressure and kinematic viscosity, respectively. The tensorial eddy-viscosity enables a selective reduction of the influence of one (or more) elements of the strain-rate tensor with respect to the corresponding physical alignment (or misalignment) between the associated principal directions. Moreover, if a perfect alignment is observed in a region of equilibrium turbulence (isotropic strain), the tensorial expression leads to a classical Boussinesq-like scalar model. A realisability condition of the present constitutive law can be established. The normal stresses have to remain positive, for $i = 1, 2, 3$, $\langle u_i u_i\rangle \geqslant 0$. This leads to the following relation: $C_{V\alpha} V^\alpha_{ii} \leqslant \frac{2}{3}$. A sufficient condition to ensure the model realisability is thus $C_{Vi} \leqslant \frac{2}{3}$, for $i = 1, 2, 3$.

A comparison between normal and shear stress anisotropy components evaluated from the PIV experiment and from modelling via (5) and measured strain tensor is presented in Fig. 6. The modelled quantities present a good agreement

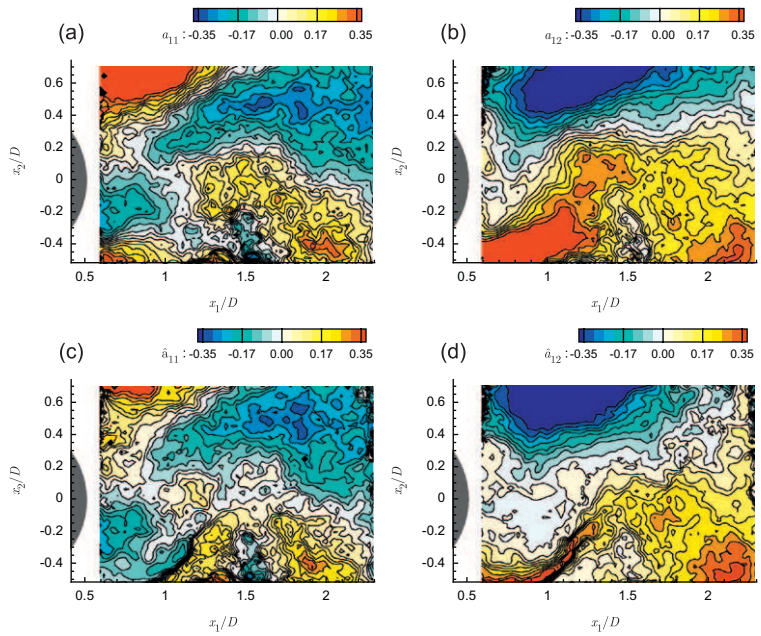

Fig. 6. Comparison between turbulent ((a) and (c)) normal and ((b) and (d)) shear stress anisotropy obtained directly from the PIV experiment ((a) and (b)), and those evaluated via expression (2) ((c) and (d)) at phase angle $\varphi = 50^\circ$.

with the experiment for both normal and shear stresses, despite slight differences in shear flow regions downstream of the separation, where the experimental uncertainties are increased. This is achieved by examining the complete phase-averaged fields at given phase angles. In Appendices A and B, a closure scheme including transport equations for the prediction of C_{V_i} coefficients is presented.

4. Numerical simulation of strongly detached flows around bodies

The present model has been implemented in the Navier–Stokes Multi-Block (NSMB) code. The NSMB solver is a numerical software of NSMB consortium solving the finite volume Navier–Stokes equations (Vos et al., 1998). Various levels of numerical schemes and turbulence modelling closures, including DES, are implemented in NSMB. In the present study, only low Mach number flows ($Ma < 0.2$) that can be regarded as incompressible are considered. In the following simulations, the space scheme is a second-order central scheme. The time scheme is a second-order backward dual time stepping scheme with constant CFL parameters and varying physical time-step ($\Delta_t \approx 5 \times 10^{-3}$ s). Solid-wall boundary conditions are imposed on the body surfaces as well as on channel walls in the cylinder test-case. Characteristic variable conditions with extrapolation in time are used on the far-field frontiers and Dirichlet conditions at the inlet. The numerical over-cost induced by the computation of the strain tensor eigen-elements at each spatial point and each timestep has been quantified in the following 2-D case. This represents approximately 15–20% of the total computation time comparing to a standard linear two-equation model. Two strongly detached flows are examined.

4.1. *Numerical simulation of the turbulent flow around a NACA0012 airfoil at high incidence and Reynolds number* 10^5

The low subsonic flow past a NACA0012 airfoil at 20° of incidence and upstream Mach number 0.18 is simulated by the present turbulence modelling. The results are compared with experiment (Berton et al., 2002) and other turbulence models. The Reynolds number based on the chord length and the free-stream velocity is 10^5. The computational grid is a C type mesh of 256×81 nodes. The flow develops a von Kármán instability and a strong vortex detachment from the leading edge. In Fig. 7, instantaneous turbulent quantities are represented. Fig. 7(a) shows the iso-contours of the turbulent kinetic energy superimposed to the streamlines. The turbulent kinetic energy has its maximum values in the shear layers downstream of the separation. It can be noticed that there is no over-production of this quantity upstream of the body as is the case in most eddy-viscosity models, with a consequent over-prediction of drag coefficient. This is achieved by an inherent local reduction of the eddy-viscosity by means of the present modelling (Fig. 7(b)). In Fig. 7(b) the directional eddy-viscosity has not been multiplied by the damping function f_μ (cf. Appendix B).

An efficient prediction of the time-averaged aerodynamic coefficients is shown by the comparison with the experiment (Table 1). This is achieved by a physically correct prediction of the turbulent kinetic energy, especially near the separation point. A number of simulations have been carried out with URANS models [k–ε Chien (Chien, 1982), k–ω SST (Menter, 1993)] as well as with the OES k–ε scheme in 2-D and 3-D, using linear eddy-viscosity modelling. Concerning URANS, both lift (C_L) and drag (C_D) coefficients are over-predicted by 2-D simulations. Concerning isotropic OES, the 3-D simulation shows an improvement. The anisotropic OES presents a good agreement with experimental data. Relative errors are $<2.5\%$ for the lift coefficient and $<2\%$ for the drag coefficient. Fig. 8 presents the prediction of the velocity in the recirculation region on the upper side of the airfoil by the present OES approach. A significant agreement with the experiment is achieved in this non-equilibrium region. These results indicate the ability of the present approach to efficiently predict strongly detached turbulent flows.

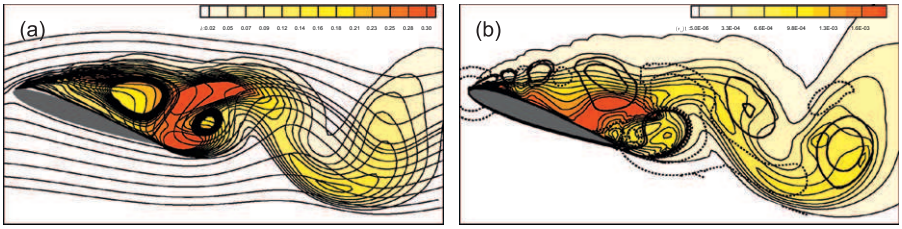

Fig. 7. Iso-contours of (a) turbulent kinetic energy and streamlines and of (b) the eddy-viscosity $(\nu_{td})_1$. In (b), iso-lines of Q criterion are superimposed ($Q = \{-6, -2, 2, 6\}$, negative values are denoted by dashed lines).

Table 1
Comparison between time-averaged aerodynamic coefficients issued from experiments (Berton et al., 2002) and numerical simulations based on first-order closure schemes

	Experiment	k–ε Chien	k–ω SST	Iso. OES k–ε 2-D	Iso. OES k–ε 3-D	AOES k–ε (present)
$\overline{C_D}$	0.32	0.33	0.365	0.36	0.33	0.325
$\overline{C_L}$	0.75	0.80	0.87	0.86	0.70	0.77

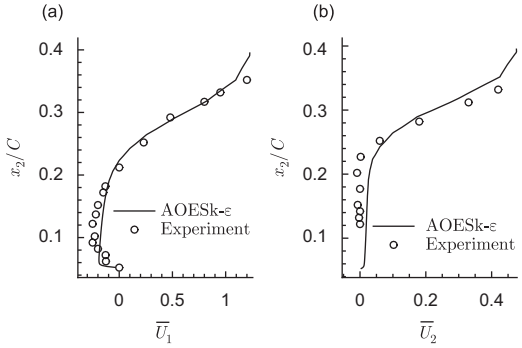

Fig. 8. Comparison between experimental (Berton et al., 2002) and numerical time-averaged velocity profiles (a) U_1 and (b) U_2 at half chord-length distance ($x_1/C = 0.508$) on the upper side of a NACA0012 airfoil at 20° of incidence and $\mathrm{Re} = 10^5$.

4.2. *Simulation of the flow around the "IMFT's circular cylinder", at Reynolds number* 1.4×10^5

The simulation of the circular cylinder flow in a confined environment (see blockage and aspect ratios in Section 2) is performed by using the OES approach in the context of the DES (Travin et al., 2000). According to this hybrid approach, statistical turbulence modelling is used in the near region, coupled with an LES modelling in the detached flow region. This is achieved by the same system of URANS equations by choosing the turbulence length scale in each elementary fluid volume of the computational grid, according to the relation: $l_{\mathrm{DES}} = \min(l_{\mathrm{RANS}}, C_{\mathrm{DES}}\Delta)$. This turbulence length scale is employed in the dissipation term of the turbulent kinetic energy transport equation and has as main result the increase of the dissipation rate with a consequent decrease of the turbulence eddy-viscosity. Δ is the largest dimension of each elementary fluid volume cell considered. C_{DES} is a constant of the model, evaluated by means of homogeneous isotropic turbulence. However, in the standard DES approach, spurious separations may occur, even in equilibrium turbulence regions (Haase et al., 2006). This inconvenient occurs because of a physical incoherence between the RANS and the LES regions, due to the fact that in standard DES, equilibrium turbulence RANS approaches are used. In the present paper, l_{RANS} turbulence length scale can be derived by the OES approach, $l_{\mathrm{DES}} = \min(l_{\mathrm{OES}}, C_{\mathrm{DES}}\Delta)$ with $l_{\mathrm{OES}} = k^{1/2}/(C_\mu\omega)$ in case of two-equation $k-\omega$ (Wilcox, 1988) modelling, with $C_{\mathrm{DES}} = 0.78$. The OES $k-\omega$ two-equation model is used with Boussinesq hypothesis (isotropic OES) to evaluate the turbulence length scale in the DES/OES approach (El Akoury et al., 2007). Therefore, the present paper aims at improving the statistical part of DES.

The computational flow domain is the same as for the experimental study presented in Section 2, to allow a rigorous comparison with the measurements. The 34-block mesh is of a reasonable size (2.4×10^6 nodes) compared to the grid that would be necessary for a full LES simulation. The results from the DES/OES approach are thus compared to the experimental data as well as to results issued from a standard DES coupled with k–ω SST model (Menter, 1993), reported by Revell et al. (2008). Because of the fact that the present flow enters the critical regime (Braza et al., 2006), the transition point is imposed at its averaged position, at the separation point. The instantaneous field of the transverse vorticity shown in Fig. 9(a) illustrates the strong 3-D character of the von Kármán mode, interspersed by a multitude of resolved smaller 3-D structures. The dimensionless frequency (Strouhal number, $\mathrm{St} = fD/U_\infty$) of the simulation is found 0.2, after FFT post-processing of the numerical results. This value is in good agreement with the experimental one (0.21). Owing to the physical reduction of the turbulence diffusion according to the OES approach, secondary instability modes of smaller wavelengths than the von Kármán one are well captured in the transverse direction. Furthermore, the shear layer instability associated with Kelvin–Helmholtz vortices clearly appears in the separated shear layers on each side of the cylinder, as shown in Fig. 9(b). It is noticeable that the majority of current modelling

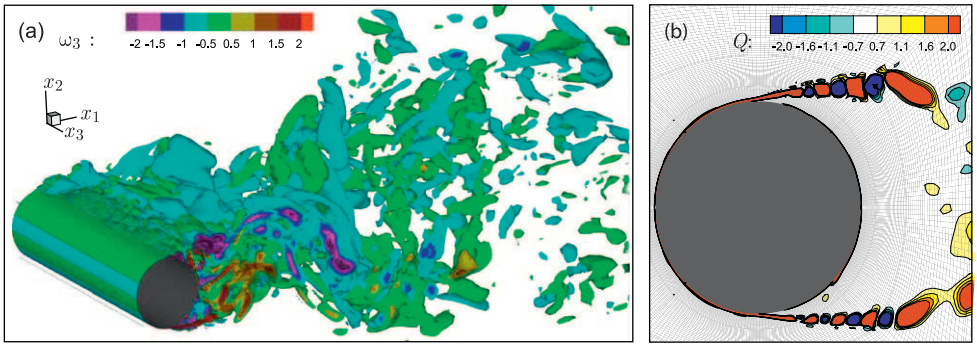

Fig. 9. Simulation of the 3-D flow around the "IMFT's circular cylinder": instantaneous (a) iso-surfaces of the transverse vorticity ω_3 and (b) iso-contours of Q criterion at half-spanwise distance allowing a precise identification of Kelvin–Helmholtz instability.

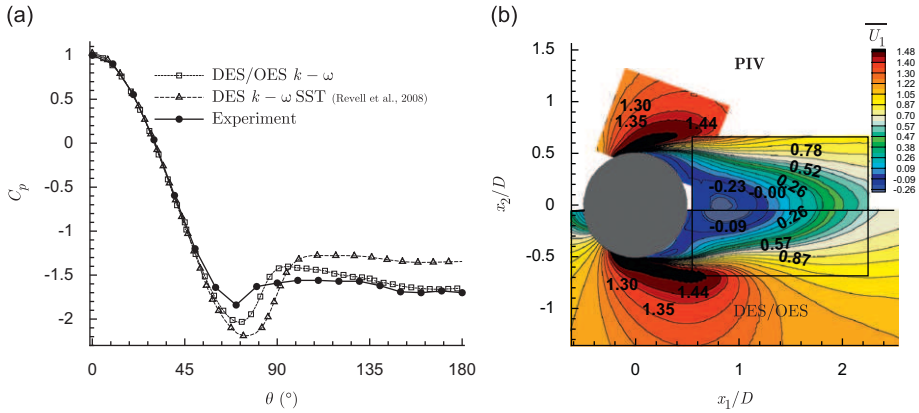

Fig. 10. Comparison between (a) the experimental and numerical time-averaged wall pressure coefficient, (b) the time-averaged longitudinal velocity fields issued form PIV and from DES/OES simulation.

approaches damp this kind of structures in the present high Reynolds number range. By tracking the Kelvin–Helmholtz vortices in the time domain, the shear layer frequency is evaluated, $f_{SL} = 5.2$. The ratio between this frequency and the Strouhal number of the von Kármán mode is therefore $f_{SL}/St = 26$.

Time-averaged quantities are shown in Fig. 10. The wall pressure coefficient simulated by means of the DES/OES method is close to the experimental one (Fig. 10(a)). In particular, the over-prediction of the low-pressure region upstream of the detachment ($\theta \approx 72°$) is reduced compared to DES k–ω SST approach and the detached region is better captured. A comparison between the mean longitudinal velocity field issued from the experiment and from the DES/OES computation is presented in Fig. 10(b). A good agreement is reached. Moreover, a reliable prediction of the time-averaged drag coefficient is achieved by the DES/OES approach, $C_D = 1.43$ (exp. $C_D = 1.44$).

Therefore, the present study shows that the use of OES in the statistical part of DES allows an improved prediction of strongly detached turbulent flows around bodies at high Reynolds number. This is achieved owing to a better coherence between the non-equilibrium RANS turbulence length scale and the LES length scale in the virtual interface regions between URANS and LES, comparing to standard DES approaches that use equilibrium turbulence RANS length scale. The results issued from the modification of DES in the sense of the OES approach are promising, especially in the perspective of an integration of the anisotropic OES modelling into hybrid methods.

5. Conclusion

In the present study, an anisotropic Organised Eddy Simulation (OES) turbulence modelling has been developed, based on a tensorial eddy-viscosity concept, for the prediction of highly detached unsteady flows around bodies in

the Reynolds number range 10^5–10^6. The non-equilibrium turbulence effects, especially stress–strain directional misalignments, have been taken into account in a first-order constitutive law founded on a tensorial eddy-viscosity. Three additional transport equations for the stress–strain projection coefficients involved in this law has been derived from the Speziale, Sarkar and Gatski second-order moment closure. The new transport equations are coupled with a two-equation model in which the anisotropic eddy-viscosity is used. The present modelling is proven efficient to simulate the 2-D detached flow around a NACA0012 at Reynolds number 10^5 with a good agreement with experiments. Furthermore, the OES approach has been successfully used in the URANS part of the hybrid Detached Eddy Simulation (DES), by adopting Boussinesq approximation as a first step. The 3-D DES/OES simulation of the flow around a circular cylinder in high blockage and aspect ratios (the "IMFT's circular cylinder" test case), at Reynolds number 1.4×10^5 emphasises the efficiency of the OES approach within DES for highly detached flows. The present modelling provides accurately the flow physics interaction with the solid wall, related to different classes of coherent structures in the near region and especially to the von Kármán and to the Kelvin–Helmholtz instability modes downstream of the separation, in the high Reynolds number range. Moreover, this is achieved by using reasonable grid sizes, an important issue for the design in fluid–structure interaction.

Acknowledgement

Part of the present work has been carried out in the DESIDER European program, no. AST3-CT-2003-502842 coordinated by EADS-Münich. The numerical implementation in NSMB was carried out in collaboration with Dr J.B. Vos and Dr Y. Hoarau who are gratefully acknowledged. The calculations were performed at the CINES and the IDRIS national computing centers, as well as on GRIDMIP network. The first author was financially supported by the Centre National de la Recherche Scientifique (CNRS) and the Délégation Générale pour l'Armement (DGA).

Appendix A. Transport equations for the stress–strain projection coefficients

From the SSG DRSM (Speziale et al., 1991), three transport equations are derived for the C_{Vi} coefficients. In a general form, the DRSM can be expressed as follows:

$$\frac{D\langle u_i u_j\rangle}{Dt} = P_{ij} + \Pi_{ij} - \varepsilon_{ij} + D_{ij}. \tag{7}$$

The production term P_{ij} is

$$P_{ij} = -k\left(\frac{4}{3}S_{ij} + a_{i\alpha}S_{j\alpha} + a_{j\alpha}S_{i\alpha} + a_{i\alpha}\Omega_{j\alpha} + a_{j\alpha}\Omega_{i\alpha}\right) \quad \text{with } \Omega_{ij} = \frac{1}{2}\left(\frac{\partial U_i}{\partial x_j} - \frac{\partial U_j}{\partial x_i}\right). \tag{8}$$

The tensorial dissipation is approximated by the isotropic expression $\varepsilon_{ij} = \frac{2}{3}\varepsilon\delta_{ij}$. The diffusion term D_{ij} contains viscous diffusion tensor D^v_{ij} and turbulent diffusion tensor D^t_{ij} defined as follows:

$$D^v_{ij} = \frac{\partial}{\partial x_\alpha}\left(\nu\frac{\partial\langle u_i u_j\rangle}{\partial x_\alpha}\right) \quad \text{and} \quad D^t_{ij} = \frac{\partial}{\partial x_\alpha}(-\langle u_i u_j u_\alpha\rangle). \tag{9}$$

D^v_{ij} is computed exactly and D^t_{ij} is modelled by Daly and Harlow (1970) extended gradient model. The pressure-strain term is modelled according to Speziale et al. (1991):

$$\begin{aligned}\Pi_{ij} = & -(c_1\varepsilon + c_1^\star P_k)a_{ij} + c_2\varepsilon(a_{i\alpha}a_{\alpha j} - \tfrac{1}{3}\delta_{ij}II_a) + (c_3 - c_3^\star II_a^{1/2})kS_{ij} + c_4k(a_{i\alpha}S_{j\alpha} + a_{\alpha j}S_{i\alpha} - \tfrac{2}{3}a_{\beta\gamma}S_{\beta\gamma}\delta_{ij}) \\ & + c_5k(a_{i\alpha}\Omega_{j\alpha} + a_{j\alpha}\Omega_{i\alpha}) \quad \text{with } II_a = a_{\alpha\beta}a_{\alpha\beta}.\end{aligned} \tag{10}$$

The constant values are given in Table 2.

Table 2
Values of the constants in Speziale, Sarkar and Gatski DRSM (Speziale et al., 1991)

c_1	$c_1^\star$	c_2	c_3	$c_3^\star$	c_4	c_5
1.7	0.90	1.05	0.8	0.65	0.625	0.2

The DRSM has been considered in its original version. The present approach can be regarded as a generalisation of the C_{as} model (Revell et al., 2006) that uses a global correlation rate between stress and strain tensors in the constitutive law. The derivative of the turbulent stress anisotropy tensor can be written as follows:

$$\frac{Da_{ij}}{Dt} = \frac{1}{k}\left(P_{ij} + \Pi_{ij} - a_{ij}(P_k - \varepsilon) - \frac{2}{3}P_k\delta_{ij}\right) + D^a_{ij}; \tag{11}$$

P_k is the turbulent kinetic energy production defined in expression (3). The global diffusion term D^a_{ij} includes both DRSM and turbulent kinetic energy diffusion terms. The transport equations for C_{Vi} are

$$\begin{aligned}\frac{DC_{Vi}}{Dt} &= -\frac{Da_{\alpha\beta}}{Dt}V^i_{\alpha\beta} - a_{\alpha\beta}\frac{DV^i_{\alpha\beta}}{Dt}\\ &= \left(\frac{4}{3} + c_3^\star II_a^{1/2} - c_3\right)V^i_{\alpha\beta}S_{\alpha\beta} + (2-2c_4)V^i_{\alpha\beta}a_{\alpha\gamma}S_{\beta\gamma} - \frac{c_2\varepsilon}{k}V^i_{\alpha\beta}a_{\alpha\gamma}a_{\gamma\beta}\\ &\quad + (2-2c_5)V^i_{\alpha\beta}a_{\alpha\gamma}\Omega_{\beta\gamma} + (1-c_1)\frac{\varepsilon}{k}C_{Vi} + (1+c_1^\star)C_{Vi}a_{\alpha\beta}S_{\alpha\beta} + \frac{c_2 II_a\varepsilon}{3k}\\ &\quad + \frac{2(c_4-1)}{3}a_{\alpha\beta}S_{\alpha\beta} - a_{\alpha\beta}\frac{DV^i_{\alpha\beta}}{Dt} + D^{C_{Vi}}.\end{aligned} \tag{12}$$

The diffusion term $D^{C_{Vi}}$ combines viscous and turbulent diffusion contributions and is approximated by

$$D^{C_{Vi}} = \frac{\partial}{\partial x_\alpha}\left(\left(\nu\delta_{\alpha\beta} + \frac{(\nu_{tt})_{\alpha\beta}}{\sigma_{C_{Vi}}}\right)\frac{\partial C_{Vi}}{\partial x_\beta}\right); \tag{13}$$

$\sigma_{C_{Vi}}$ coefficients are set to the value of one. Moreover the second term issued from the derivation of C_{Vi}, vanishes if the anisotropy tensor is replaced by its approximation, $\hat{\boldsymbol{a}}$: $-\hat{a}_{\alpha\beta}DV^i_{\alpha\beta}/Dt = 0$.

Appendix B. Summary of the OES anisotropic first-order model

Three transport equations have been derived from DRSM to close the anisotropic constitutive law defined by expression (5). These have been developed to be coupled with standard two-equation models since k and ε appear explicitly in the r.h.s. of Eq. (12). The corresponding anisotropic first-order closure scheme thus involves five equations in addition to the three momentum equations (6) in the general 3-D incompressible case: two transport equations for k and ε and three for C_{Vi}. The scalar eddy-viscosity is replaced by the tensorial one (4) in the whole system. The OES turbulence damping function is used (Table 3). The anisotropic OES k–ε scheme thus consists in solving Eqs. (4), (5) and (12) jointly to the two following:

$$\frac{Dk}{Dt} = \frac{\partial}{\partial x_\alpha}\left(\left(\nu\delta_{\alpha\beta} + \frac{(\nu_{tt})_{\alpha\beta}}{\sigma_k}\right)\frac{\partial k}{\partial x_\beta}\right) + P_k - \varepsilon - \frac{2\nu k}{y_n^2}, \tag{14}$$

$$\frac{D\varepsilon}{Dt} = \frac{\partial}{\partial x_\alpha}\left(\left(\nu\delta_{\alpha\beta} + \frac{(\nu_{tt})_{\alpha\beta}}{\sigma_\varepsilon}\right)\frac{\partial \varepsilon}{\partial x_\beta}\right) + c_{\varepsilon_1}f_1\frac{\varepsilon}{k}P_k - c_{\varepsilon_2}f_2\frac{\varepsilon^2}{k} - \frac{2\nu\varepsilon}{y_n^2}\exp(-0.5y^+). \tag{15}$$

Damping functions and constants are given in Table 3.

In the 2-D case, only three equations are needed for turbulence modelling since $C_{V2} = -C_{V1}$.

Table 3
Damping functions and constant parameters of the present OES anisotropic model

f_μ	f_1	f_2	c_{ε_1}	c_{ε_1}	σ_k	σ_ε
$1-\exp(-0.0002y^+ - 0.000065y^{+2})$	1	$1-0.22\exp\left(-\frac{k^2/(\varepsilon\nu)^2}{36}\right)$	1.44	1.92	1	1.3

References

Berton, E., Allain, C., Favier, D., Maresca, C., 2002. Experimental methods for subsonic flow measurements. In: Notes on Numerical Fluid Mechanics and Multidisciplinary Design, vol. 81, Springer, New York, pp. 97–104

Bouhadji, A., Bourdet, S., Braza, M., Hoarau, Y., Rodes, P., Tzabiras, G., 2002. Turbulence modelling of unsteady flows with a pronounced periodic character. In: Notes on Numerical Fluid Mechanics and Multidisciplinary Design, vol. 81, Springer, New York, pp. 87–96.

Bourdet, S., Braza, M., Hoarau, Y., El Akoury, R., Ashraf, A., Harran, G., Chassaing, P., Djeridi, H., 2007. Prediction and physical analysis of unsteady flows around a pitching airfoil with the dynamic mesh approach. European Journal of Mechanics—B/Fluids 16 (3/4), 451–476.

Bourguet, R., Braza, M., Perrin, R., Harran, G., 2007. Anisotropic eddy-viscosity concept for strongly detached unsteady flows. AIAA Journal 45 (5), 1145–1149.

Boussinesq, J., 1877. Théorie de l'écoulement tourbillant. Mémoires présentés par divers savants à l'Académie des Sciences de Paris, France, vol. 23, pp. 46–50.

Braza, M., Perrin, R., Hoarau, Y., 2006. Turbulence properties in the cylinder wake at high Reynolds number. Journal of Fluids and Structures 22, 755–771.

Carpy, S., Manceau, R., 2006. Turbulence modelling of statistically periodic flows: synthetic jet into quiescent air. International Journal of Heat and Fluid Flow 27, 756–767.

Chien, K.Y., 1982. Predictions of channel and boundary-layer flows with a low-Reynolds-number turbulence model. AIAA Journal 20 (1), 33–38.

Daly, B., Harlow, F., 1970. Transport equations in turbulence. Physics of Fluids 13, 2634–2649.

Davidson, L., Cokljat, D., Fröhlich, J., Leschziner, M.A., Mellen, C., Rodi, W., 2003. LESFOIL: large eddy simulation of flow around a high lift airfoil. In: Notes on Numerical Fluid Mechanics and Multidisciplinary Design, vol. 83, Springer, Berlin.

Durbin, P.A., Pettersson Reif, B.A., 2001. Statistical Theory and Modeling for Turbulent Flow. Wiley, New York.

El Akoury, R., Braza, M., Hoarau, Y., Vos, J.B., Harran, G., Sévrain, A., 2007. Unsteady flow around a NACA0021 airfoil beyond stall at 60° angle of attack. In: Proceedings of the IUTAM Symposium on Unsteady Separated Flows and their Control, June 18–20, Corfu, Greece, Springer, in press.

Gatski, T.B., Speziale, C.G., 1993. On explicit algebraic stress models for complex turbulent flows. Journal of Fluid Mechanics 254, 59–78.

Haase, W., Aupoix, B., Bunge, U., Schwamborn, D., 2006. FLOMANIA—a European initiative on flow physics modelling. In: Notes on Numerical Fluid Mechanics and Multidisciplinary Design, vol. 94, Springer, New York.

Hoarau, Y., Perrin, R., Braza, M., Ruiz, D., Tzabiras, G., 2006. Advanced in turbulence modelling for unsteady flows. In: Notes on Numerical Fluid Mechanics and Multidisciplinary Design, vol. 94, Springer, New York, pp. 85–88.

Hunt, J.C., Wray, A., Moin, P., 1988. Eddies, stream, and convergence zones in turbulent flows. Center for Turbulence Research Report, CTR-S88, Stanford, CA, USA.

Jin, G., Braza, M., 1994. A two-equation turbulence model for unsteady separated flows around airfoils. AIAA Journal 32 (11), 2316–2320.

Launder, B.E., Reece, G.J., Rodi, W., 1975. Progress in the development of a Reynolds stress turbulence closure. Journal of Fluid Mechanics 68, 537–566.

Menter, F.R., 1993. Zonal two equation k–ω turbulence models for aerodynamic flows. AIAA Paper 2906.

Peng, S.-H., Haase, W., 2008. Advances in hybrid RANS-LES modelling. In: Notes on Numerical Fluid Mechanics and Multidisciplinary Design, vol. 97, Springer, New York.

Perrin, R., Cid, C., Cazin, S., Sevrain, A., Braza, M., Moradei, F., Harran, G., 2007. Phase-averaged measurements of the turbulence properties in the near wake of a circular cylinder at high Reynolds number by 2C-PIV and 3C-PIV. Experiments in Fluids 42 (1), 93–109.

Pope, S.B., 1975. A more general effective-viscosity hypothesis. Journal of Fluid Mechanics 72, 331–340.

Revell, A.J., Benhamadouche, S., Craft, T., Laurence, D., 2006. A stress–strain lag eddy viscosity model for unsteady mean flow. International Journal of Heat and Fluid Flow 27 (5), 821–830.

Revell, A.J., Benhamadouche, S., Craft, T., Laurence, D., 2008. Turbulence modelling of strongly detached unsteady flows: the circular cylinder. In: Notes on Numerical Fluid Mechanics and Multidisciplinary Design, vol. 97, Springer, New York, pp. 279–288.

Shih, T.B., Zhu, J., Lumley, J.L., 1993. A realizable Reynolds stress algebraic equation model. NASA TM 105993, ICOMP 92-27, CMOTT 92-14.

Speziale, C.G., Xu, X.H., 1996. Towards the development of second-order closure models for non-equilibrium turbulent flows. International Journal of Heat and Fluid Flow 17, 238–244.

Speziale, C.G., Sarkar, S., Gatski, T.B., 1991. Modeling the pressure strain correlation of turbulence: an invariant dynamical systems approach. Journal of Fluid Mechanics 227, 245–272.

Travin, A., Shur, M., Strelets, M., Spalart, P., 2000. Detached Eddy simulations past a circular cylinder. Journal of Flow Turbulence and Combustion 63, 293–313.

Vos, J.B., Chaput, E., Arlinger, B., Rizzi, A., Corjon, A., 1998. Recent advances in aerodynamics inside the NSMB (Navier–Stokes Multi-Block) consortium. In: 36th Aerospace Sciences Meeting and Exhibit, AIAA P. 0802, Reno, USA.

Wilcox, D.C., 1988. Re-assessment of the scale-determining equation for advanced turbulence models. AIAA Journal 26 (11), 1414–1421.